Biomimetic electro-oxidation of alkyl sulfides from exfoliated molybdenum disulfide nanosheets

Lahcene Maachou, Kun Qi, Eddy Petit, Zhaodan Qin, Yang Zhang, Didier Cot, Valérie Flaud, Corine Reibel, Heba El-Maghrbi, Lei Li, et al.

ARTICLE

Biomimetic Electro-oxidation of Alkyl Sulfides from Exfoliated Molybdenum Disulfide Nanosheets

Received 00th January 20xx,
Accepted 00th January 20xx

DOI: 10.1039/x0xx00000x

Lahcene Maachou,[a†] Kun Qi,[a†] Eddy Petit,[a] Zhaodan Qin,[a] Yang Zhang,[a] Didier Cot,[a] Valérie Flaud,[b] Corine Reibel,[b] Heba El-Maghrabi,[a] Lei Li,[c] Philippe Miele,[a] Daniel Kaplan,[d] Manish Chhowalla,[e] Nicolas Onofrio,[f] Damien Voiry*[a]

Enzymes are biological catalysts that are interesting for key reactions such as hydrogen evolution, CO_2 conversion into hydrocarbons and the fixation of nitrogen. Enzymes are particularly good catalysts for organic reactions because of their high selectivity. However, they exhibit modest stability and require extensive purification, which makes them costly. Here, we report a biomimetic electroactive two-dimensional (2D) catalyst based on single-layer metallic MoS_2 nanosheets for the oxidation of alkyl and aryl sulfides. The structure of the MoS_2 nanosheets mimics the active site of natural dimethyl sulfoxide (DMSO) reductase found in anaerobic bacteria. We demonstrate that 2D MoS_2 nanosheets efficiently oxidize organic sulfides. Notably, we show that dimethyl sulfide can be electro-oxidized to DMSO with activity surpassing that of noble metal catalysts. The production of DMSO using metallic 1T' phase MoS_2 reaches 680 L h^{-1} per gram at 1500 mV vs. NHE – ~ 4 times higher than platinum nanoparticles – and is stable for > 24 hours. Our findings provide new directions for electrosynthesis from metallic 2D materials.

Introduction

Enzymes are proteins that catalyze key reactions in living organisms.[1] They possess high selectivity, which makes them attractive for enantioselective synthesis of drug molecules in the pharmaceutical industry.[2,3] The catalytically active sites on enzymes typically consist in coordinated transition metals and recent insights into how they catalyze reactions has enabled progress in the design of novel bio-inspired electrocatalysts.[4] For example, understanding of mechanisms that are responsible for hydrogenase activity has allowed the development of electro-active molecular catalysts with structures that reproduce active sites of the natural enzyme.[5] Nanozymes are nanomaterials with enzyme-like characteristics with superior stability compared to natural proteins – making them attractive as electro-catalysts with tunable activity.[6,7] Since the discovery of unexpected peroxidase-like activity of iron oxide nanoparticles,[8] various nanozymes have been realized using metal oxides, noble metals, graphene and derivatives, and metal-organic frameworks (MOFs).[9–11] However, two outstanding challenges remain: first, nanozymes show much lower catalytic activity because of the low densities of active sites;[12] and second, the inhomogeneous composition and crystal facet structure[13] make it difficult to identify the active sites. These bottlenecks are significant hurdles for implementation of nanozymes in applications.

Exfoliated two-dimensional (2D) materials are known to be good electrocatalysts.[14] In particular, transition metal dichalcogenides (TMDs) have been widely studied for their catalytic properties in reactions such as the hydrogen evolution reaction, as well as oxygen and CO_2 reduction reactions.[15–17] Despite the large body of work on catalysis with 2D materials, their application in electrosynthesis of organic molecules has yet to be explored. Oxidation of organic sulfide compounds into sulfoxides for production of drugs such as esomeprazole and armodafinil are important reactions in the pharmaceutical industry.[18,19] With an annual production of approaching 100,000 metric tons, dimethyl sulfoxide (DMSO) is widely used as polar and aprotic organic solvent in pharmaceutical and microelectronic industry as well as an intermediate for the synthesis of sulfur-based derivative molecules. Contrary to thiols, organic sulfide are stable in air and the industrial process for the synthesis of sulfoxide relies on the use of undesirable strong oxidizing agents including NO_X or peroxy acids.[20,21] Redox processes can be used to oxidize organic sulfides at room temperature and without the use of harsh chemicals – greatly limiting the safety concerns. However, only handful contributions have been reported on the electro-oxidation of DMS in dimethylsulfoxide and dimethylsulfone using platinum

a. *Institut Européen des Membranes, IEM, UMR 5635, University of Montpellier, ENSCM, CNRS, 34095 Montpellier Cedex5, France*
b. *Institut Charles Gerhardt, ICGM, UMR 5253, University of Montpellier, ENSCM, CNRS, 34095 Montpellier Cedex5, France*
c. *College of Biological, Chemical Sciences and Engineering, Jiaxing University, Jiaxing, Zhejiang 314001, China*
d. *US Army CCDC-AC RDECOM-ARDEC, Advanced Materials Technology Branch, Picatinny Arsenal, New Jersey 07806, USA*
e. *Department of Materials Science & Metallurgy, University of Cambridge, Cambridge, UK*
f. *Department of Applied Physics, The Hong Kong Polytechnic University, Hong Kong, China*
† These authors contributed equally.
Electronic Supplementary Information (ESI) available: [details of any supplementary information available should be included here]. See DOI: 10.1039/x0xx00000x

as anode.[22,23] The use of expensive and scarce noble metals therefore limits practical applications.

In this work, we report metallic two-dimensional MoS_2 as biomimietic catalyst with intrinsic enzyme-like active sites for the electro-oxidation of organic sulfides. The atomic structure of MoS_2 resembles that of the DMSO reductase active site – an enzyme responsible for reversible reduction of DMSO in DMS. When tested in oxygen-saturated, non-aqueous electrolyte solution, DMS is electrochemically converted to DMSO on the MoS_2 nanosheets with activity and selectivity superior to those of noble metals. Our results show that the production of DMSO from the electrochemical oxidation of DMS using 1T' MoS_2 nanosheet catalysts is significantly higher (680 L h-1 per gram) than for Pt nanoparticle catalysts (210 L h^{-1} g^{-1}). Our numerical predictions suggest that the superior activity is ascribed to the lower binding energy of DMS on the basal plane and the edge sites of the 1T' phase.

Results and discussion

Chemically exfoliated MoS_2 nanosheets

MoS_2 nanocrystals are known catalysts for the oxidation of sulfur-based molecules. For example, Lauristen et al. have observed thiophene adsorption at the brim sites on sulfide MoS_2 crystals, suggesting that such sites can play an active role in catalysis.[24] Catalytic oxidation of thiols into disulfides has also been achieved – hinting at nanozyme-like activity of MoS_2 for oxidation of sulfur-based molecules.[25] Recently MoS_2 with inclusion of cobalt single-atom have been proposed for the heterogeneous oxidation of organic sulfide using H_2O_2 as oxidizing agent.[26] Alternatively, DMSO can be prepared from the oxidation of DMS with a standard potential of 574 mV vs. NHE in water but the reaction suffers from large overpotential and possible degradation of the catalyst materials **(Figure S1)**.[27] The similarity between the active sites of hydrogenase and the structure of MoS_2 edges led to its use as an HER catalyst.[5] DMSO reductase (DMSOR) – an enzyme produced under anaerobic conditions in some bacteria – is known to reversibly reduce DMSO into DMS. In contrast to hydrogenase that contains Fe and Mo metals, DMSOR active site consists only of molybdenum Mo(VI) coordinated with 4 sulfur atoms from two pyranopterin dithiolene ligands (**Figures 1a,b**). We synthesized the 1T' and 2H MoS_2 nanosheets using our previously reported intercalation-assisted exfoliation method (**Figure 1c,d**) (See Experimental Section).[28,29] The nanosheets were exfoliated in water and first characterized by atomic force microscopy **(Figure 1e)**. The size distributions extracted from the AFM measurements reveal that the nanosheets are ≈ 200nm in length while the average thickness is ≤ 1 nm, consistent with single layer nanosheets (**Figure 1f**). It is well known that as-synthesized nanosheets by chemical exfoliation possess the 1T' phase structure.[30] The 2H phase is obtained by mild annealing (at 300°C under 5% H_2 in argon, See Experimental Section) of the 1T' phase MoS_2 nanosheets) of the as-synthesized nanosheets.[29,30] From the deconvolution of the XPS spectra

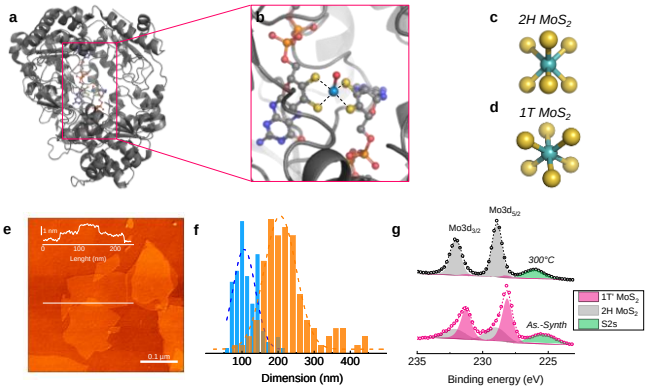

Figure 1. *Characterization of chemically exfoliated MoS_2 nanosheets. (a) Structural model of DMSO reductase enzyme. (b) Structure of the active sites of the DMSO reductase showing the molybdenum atom coordinated with two pyranopterin dithiolene ligands. Color code for the atoms: grey: C, green: Mo, yellow: S, orange: P, red: O, blue: N. (c,d) 2H and 1T' phase of MoS_2 with Mo atoms in a trigonal prismatic and octahedral coordination with sulfur atoms. (e) Mixed topographic and phase image obtained by using atomic force microscopy (AFM). Inset: height profile of an individual exfoliated MoS_2 nanosheet deposited on 300 nm SiO_2/Si wafer. (f) Length (orange) and width (blue) distributions of the exfoliated MoS_2 nanosheets measured by AFM. The Gaussian fits of the length and width distribution are shown as dashed line. (g) X-ray photoelectron spectroscopy of the Mo 3d regions of as-exfoliated and 300°C-annealed MoS_2 nanosheets. The raw and the fitted data are shown with open symbols and dashed lines respectively. From the deconvolution of the raw XPS signals, the metallic 1T' polymorph composes 70% of as-exfoliated nanosheets. At the opposite, the annealed nanosheets consist in 95% of the semiconducting 2H polymorph.*

from the Mo3d and S2p regions, we have estimated the 1T' phase concentration in the as-exfoliated nanosheets to be ≈ 75%, while the 2H phase is almost entirely restored after annealing.[29] The presence of the 1T' and 2H phases is also detected in Raman of as-exfoliated and annealed MoS_2 nanosheets (**Figure S2**).

The catalysts were prepared by loading a controlled amount of 1T' phase MoS_2 nanosheets on the electrode via drop casting and controlled evaporation of the solvent.[29] Scanning electron microscopy (SEM) on the electrode reveals that the nanosheets are densely packed on the surface without significant porosity (**Figure 2a**). The 2H MoS_2 electrode is virtually identical (Inset **Figure 2a**) – meaning that the phase transition during mild annealing does not affect the orientation or morphology of thenanosheets so that only the phase of MoS_2 is modified. Next, we determined the electrochemically active surface area (ECSA) by estimating the double layer capacitance (C_{dl}) of 1T'- and 2H MoS_2 electrodes (See "Estimation of the double layer capacitance for MoS_2 nanosheets and Pt nanoparticles" in the Experimental Section). To do this, different electrodes were cycled in 0.1M tetraethylammonium tetrafluoroborate (NEt_4BF_4) in acetonitrile at increasing scan rates from 5 to 200 mV s^{-1} (**Figure 2b,c**). The double layer capacitances from the 1T' and 2H electrodes were found to be 284 and 55 µF cm^{-2}, respectively (**Figure 2d**). Assuming a C_{dl} of ≈ 10 µF cm^{-2} for ideally flat MoS_2 in organic electrolytes, [32] the ECSA is estimated to 28.4 cm^{-2}_{ECSA} and 5.5 cm^{-2}_{ECSA} for electrodes with 1T' and 2H phases, respectively. The reduction of the ECSA values between 1T' and 2H phases MoS_2 is likely due to the decrease in the interlayer spacing of the nanosheets after annealing and therefore limited intercalation of ions in the 2H MoS_2 electrodes as reported in

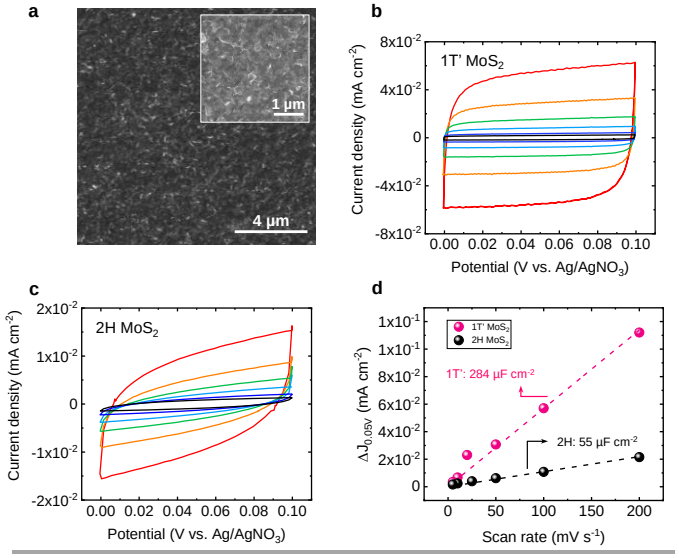

Figure 2. *Characterization of the MoS_2 electrodes. (a) Top view of the MoS_2 electrodes observed under scanning electron microscope (SEM). (b,c) Cyclic voltammetry curves of the 1T' phase (b) and the 2H phase (c) of MoS_2 nanosheets deposited on glassy carbon electrodes measured at increasing scan rates from 5 to 200 mV s^{-1}. (d) Corresponding evolution of $\Delta J_{0.05V}$ with the scan rates for the 1T' and 2H phase MoS_2. The slope gives access to the double layer capacitance (C_{dl}) of the MoS_2 electrodes.*

Ref .[33] The C_{dl} is also significantly lower in organic electrolyte than in aqueous electrolytes (**Figure S3**) due to nature of electrochemically active sites being different for different types of electrolyte solutions.

Electrochemical activity of MoS_2 nanosheets towards the oxidation of DMS

The electrochemical responses from 1T' and 2H MoS_2 nanozymes were measured in 0.1 M NEt_4BF_4 in acetonitrile and the applied potentials corrected versus Normal Hydrogen Electrode (NHE) after calibrating the reference electrode using ferrocene: Fc/Fc^+ (**Figure S5**). The electrolyte solution was saturated with O_2 used as a source of oxygen for the reaction. When sweeping the potential of the working electrodes, the anodic current density rapidly and continuously increased for both phases of MoS_2 nanosheets (**Figure 3a**). The onset potential (the potential at which the Faradaic current begins to increase) from the 1T' phase was found to be 1190 mV vs. NHE – clearly lower than the onset potential of 2H phase of MoS_2 (1280 mV vs. NHE). To confirm that the anodic current is solely due to the oxidation of DMS, we performed the same experiment but in the absence of DMS. Virtually no current wasdetected without – confirming that the anodic current is due to the reaction of DMS and not the oxidation of the catalyst itself (**Figure S6**). To further quantify the catalytic performance of the MoS_2 nanosheets with respect to state-of-the art catalysts, we compare the results with 60 mesh palladium: Pd-NP, Polycrystalline platinum: Pt-PolyC, commercial platinum nanoparticles supported on porous carbon (20% in mass): Pd-NP and a dirhodium(II) carboxylate complex: $Rh_2(esp)_2$ (esp=α, α',α', α'-tetramethyl-1,3-benzenedipropionic acid) that is a known catalysts for the oxidation of organic sulfides.[34] The results reveal that the 1T' phase of MoS_2 catalysts exhibit geometrical current density of 9.2 mA $\mathrm{cm}^{-2}_{\mathrm{geom}}$ at 1400 mV vs. NHE compared to 4.3 mA $\mathrm{cm}^{-2}_{\mathrm{geom}}$ for Pt nanoparticle electrodes (Figure 3a). 1T' MoS_2 catalysts also outperforms Pt nanoparticles, palladium and dirhodium complex with a lower onset potential of ≈ 45 mV, 150 mV and 160 mV respectively (Inset Figure 3a). The substantially better electrocatalytic activity of 1T' phase MoS_2 is also supported by Tafel plots shown in **Figure 3b**. The Tafel slope of 1T' MoS_2 reaches 75 mV dec^{-1}. For comparison Tafel slopes of 99 mV dec^{-1}, 110 mV dec^{-1}, 125 and 115 mV dec^{-1} are obtained for 2H MoS_2, Pt nanoparticles, Pd and dirhodium respectively. The reduced Tafel slope is attributed to the improved electrocatalytic reaction kinetics due to higher electrical conductivity of metallic 1T' phase of MoS_2. [31,35]

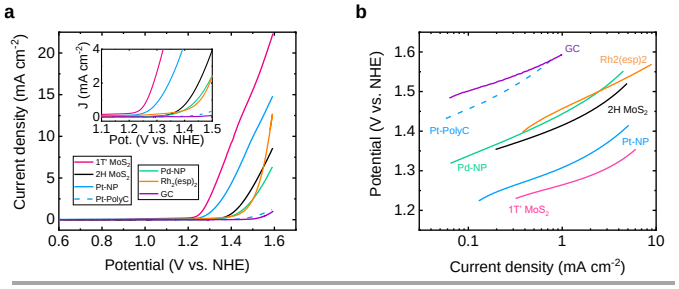

Figure 3. *Electrocatalytic behavior of MoS_2 electrodes towards the oxidation of DMS compared with reference catalysts. (a) Polarization curves of 1T' and 2H MoS_2 nanosheets in presence DMS compared to platinum nanoparticles, polycrystalline platinum, palladium nanoparticles, $Rh_2(esp)_2$ and glassy carbon. Inset: Magnification of the low potential region. Scan rate: 20 mV s^{-1}. (b) Corresponding Tafel plots from the different MoS_2 electrodes compared to platinum. The smallest values of Tafel slopes are obtained for 1T' MoS_2 nanosheets with 75 mV dec^{-1}.*

To assess the true electrocatalytic activity of MoS_2 nanosheets for the reduction of DMS, we normalized the geometrical current to the ECSA values obtained from the C_{dl} measurements. We determined the surface of platinum exposed to the electrolyte for both polycrystalline Pt and Pt nanoparticles using the copper underpotential deposition (Cu-UPD) method developed by Green and Kucernak.[36] Under UPD conditions at +0.3 V vs. RHE, Cu is solely deposited on the active Pt while no copper is deposited on the carbon support. The density of active sites on Pt was determined from the exchanged charges when stripping Cu monolayers deposited on Pt nanoparticles: Q_{Strip}. Assuming 420 µC cm^{-2} of charges exchanged for the deposition of a monolayer of Cu on Pt,[36] the active surfaces for polycrystalline Pt and Pt nanoparticles were estimated to 4.14 and 14.8 $\mathrm{cm}^2/\mathrm{cm}^2_{\mathrm{Geom}}$ ("Cu Underpotential Deposition" section in the Supporting Information and **Figure S7**). We note that while the Cu UPD method has been developed for unsupported platinum, we found that the surface area of the Pt nanoparticles reaches 10 m^2 g^{-1} of catalyst, which is close to the values for unsupported Pt nanoparticles.[36] **Figure 4a** shows the ECSA-normalized current density ($J_{ECSA} = \frac{J_{Geom}}{ECSA}$) of the different electrodes. The normalized current density for 1T' and 2H MoS_2 reach 0.32 and 0.13 mA cm^{-2}_{ECSA} at 1400 mV vs. NHE respectively. A lower onsetpotential is observed from the 1T' MoS_2, while J_{ECSA} increases faster in the case of 2H MoS_2. More importantly, the ECSA-normalized current density from MoS_2

electrodes is almost one order of magnitude higher than that of the polycrystalline Pt electrode at 0.02 mA cm_{ECSA}^{-2} at the same applied potential (Figure 4a). MoS_2 also compares favorably with Pt nanoparticles that exhibit a current density of 0.28 mA cm_{ECSA}^{-2} for the reaction (Inset Figure 4a). We performed electrochemical impedance spectroscopy (EIS) on electrodes of the different phases of MoS_2 as well as Pt nanoparticles (**Figure 4b**). The EIS measurements were performed at onset potentials of 1300 and 1350 mV vs. NHE. The impedance responses consist of 2 semi-circles corresponding to the electrolyte response for the highest frequencies and the reaction responses for the lower frequencies. The high frequency responses in the form of quasi semi-circles are independent of the applied potential at the working electrode and are attributed to the responses from the counter electrode, substrate-catalyst interface and the electrolyte.[37] The second semi-circle originates from the working electrode and originated from the charge transfer resistance (R_{CT}) and the capacitances. The equivalent circuit used for fitting the EIS data is shown in inset of Figure 4b. The values of R_{CT} decrease when the applied potential is increased, reflecting improved reaction kinetics (**Figure S8a, b** and **Table S1**). At 1300 mV vs. NHE, the charge transfer resistance is estimated to be ~ 370 Ω for 1T' MoS_2, which is lower than the values extracted for 2H MoS_2 (1480 Ω) and Pt nanoparticles (~ 790 Ω).

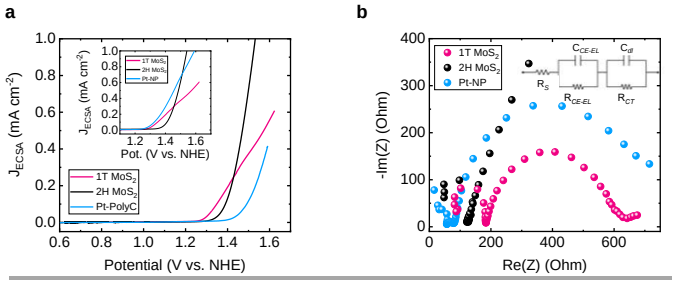

Figure 4. *Comparison of the electrochemical responses from MoS_2 nanosheets and platinum. (a) ECSA-normalized polarization curves for the DMS oxidation on MoS_2 nanosheets and polycrystalline platinum (Pt-PolyC). Inset: Comparison between the 1T' and 2H MoS_2 nanosheets with supported Pt nanoparticles (Pt-NP). (b) Nyquist plots of the 1T' and 2H MoS_2 nanosheets as well as Pt nanoparticles measured at 1350 mV vs. NHE.*

Quantification of DMSO production and estimation of Faradic efficiency

Next, we investigated the product of the DMS oxidation reaction by holding the potential of the electrode at 1500 mV vs. NHE. The products of the reaction after 4, 8 and 24 hours were analyzed using nuclear magnetic resonance (See "Detection of the products of the reaction via Nuclear magnetic resonance (NMR)" section in the Supporting Information). According to the literature, the oxidation of DMS can form several products including dimethyl sulfoxide, dimethyl sulfone and methyl sulfonates.[38,39] In our NMR measurements, DMS and DMSO signatures are clearly identified at 2.08 ppm and 2.5 ppm respectively (**Figure 5a**). The NMR peaks from dimethyl sulfone and methyl sulfonates – expected at 2.91 and ~ 3.1 ppm – are not detected even after 24 hours of reaction (**Figure S10**). These results demonstrate that the electrochemical oxidation of DMS on the MoS_2 nanozymes is highly selective towards the formation of DMSO. We note that as the reaction proceeds, the DMSO signals increase continuously with time while the signatures for DMS decrease. **Figure 5b** shows the production of DMSO over 24 hours from MoS_2 and platinum electrodes. The production of DMSO from the 1T' phase of MoS_2 is largely maintained up to 24 hours with a total production of 250 mol g^{-1}, equivalent to a production rate of 680 L h^{-1} per gram of catalyst (Inset Figure 5b). This performance is clearly higher than that of 2H MoS_2 and Pt nanoparticles that exhibit a production of 30 and 71 mol g^{-1} after 24 hours equivalent to ≈ 89 L h^{-1} g^{-1} and ≈ 210 L h^{-1} g^{-1}, respectively. More importantly our results also demonstrate that 1T' MoS_2 can sustain high production rate of DMSO with a quasi linear increase of the evolved DMSO, while the production rates from Pt and 2H MoS_2 tend to stabilize after 4 hours of reaction. This demonstrates that 1T' MoS_2 does not suffer from rapid deactivation of its catalytic properties compared to Pt or 2H MoS_2.

To obtain fundamental insight on the mechanisms of the reaction, we have estimated the quantity of electrons involved

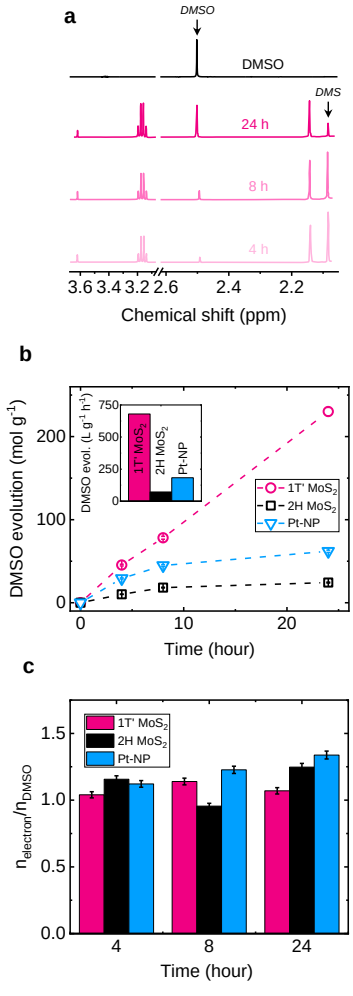

Figure 5. *Production ratio of DMSO and determination of the reaction efficiency. (a) NMR spectra of the electrolyte during the reaction after 4, 8 and 24 hours. The DMSO and DMS signatures are visible at 2.1 ppm and 2.5 ppm respectively. (b) DMSO production from the 1T' and 2H MoS_2 electrodes compared with supported Pt nanoparticles. Inset: Production rates of DMSO for the different electrodes averaged over 24 hours. (c) Ratio: n_{e^-} : n_{DMSO} obtained from the NMR results and*

the electrochemical measurements for the 3 different electrodes after 4, 8 and 24 hours.

per molecule of DMSO formed. We found that the ratio: n_{e^-}: n_{DMSO} is the slowest for 1T' MoS_2 confirming the high efficiency of the 1T' phase. That is, after 24 hours, both 1T' and 2H phase demonstrate a lower n_{e^-}: n_{DMSO} ratio than Pt nanoparticles with 1.07 and 1.25 electrons per DMSO molecule, respectively, compared to 1.34 for Pt nanoparticles. Assuming one electron involved in the reaction, the Faradaic efficiency for the initial 4 hours of reaction is close to 96.2±2.1 % for 1T' phase MoS_2 and 86.4±1.8 for the 2H MoS_2 compared to 89.1±1.9 % for Pt nanoparticles (**Figure 5c**). After 24 hours, the Faradaic efficiency (FE) is largely maintained for 1T' MoS_2 (97%) and 2H MoS_2 (92 %) – in contrast to Pt nanoparticle catalysts where the FE retention drops to 83.8%. To confirm the stability of the MoS_2 nanosheets, the electrodes were characterized using Raman and XPS spectroscopy (**Figure S11**)[40,41]. The signatures from the 1T' phase are clearly visible from the E_{1g}, J_1 and J_3 peaks as well as from the deconvolution of the Mo3d and S2p XPS spectra. Importantly virtually no signals from the oxidized Mo and S are detected in XPS, while the 1T' phase is estimated to ~50 % after the reaction, suggesting minimal relaxation of the metallic structure.

Estimation of intrinsic activity of 1T' and 2H MoS_2 nanozymes towards the oxidation of DMS

To benchmark activity of 1T' and 2H phases of MoS_2 with that of platinum towards oxidation of DMS, we normalized the activity per mass of catalysts loaded on the electrode. **Figure 6a** shows the FE-normalized mass activity of MoS_2 compared to Pt nanoparticles. At 1400 mV vs. NHE, the activity of 1T' MoS_2 nanosheets reaches 240 A g^{-1} – compared to 16.4 A g^{-1} for 2H

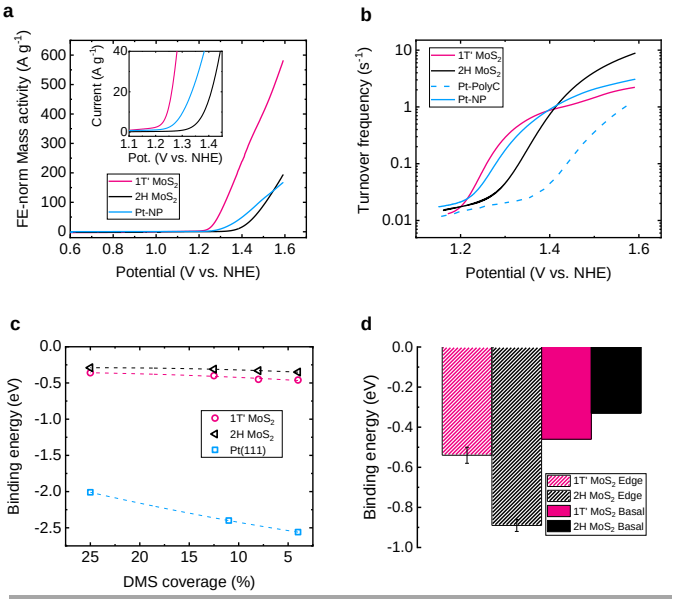

Figure 6. *Estimation of the electrocatalytic performance of MoS_2 nanosheets towards DMSO oxidation. (a) Evolution of the mass activity (in A g^{-1}) with the increase of the applied potential for 1T' and 2H MoS_2 electrodes compared to 20% Pt/C. The mass activity is normalized by the faradaic efficiency. (b) Evolution of the Turnover frequency (TOF) with the onsetpotential for 1T' and 2H MoS_2 nanosheets and compared to polycrystalline Pt. (c) Binding energy of DMS on the surface of MoS_2 and Pt (111) as a function of the coverage fraction. (d) Comparison between the binding energy of DMS at the Mo 100%S-edges and the basal planes of the 1T' and 2H phases of MoS_2.*

MoS_2 nanosheets. The DMS oxidation performance of the 1T' polymorph is 5-fold larger than for Pt nanoparticles supported on carbon. The required potential to generate a current of 50 A g^{-1} (equivalent to 132 L g^{-1} h^{-1}) is 1280 mV vs. NHE – 120 mV lower than in the case of Pt nanoparticles. To further evaluate the intrinsic electrocatalytic properties of the MoS_2 nanosheets, we estimated the turnover frequency (TOF) based on ECSA measurements and assuming active site density of 1.5×10^{15} cm^{-2} for a flat MoS_2 surface. We note that for the calculations of the TOF, we assume that the whole surface of the MoS_2 nanosheets is active. The TOF values from the 1T' and 2H phases were compared to those from the platinum nanoparticles (**Figure 6b**). The density of active sites for platinum was estimated from UPD measurements and assuming a site density of 1.1×10^{15} cm^{-2}.[42] The higher intrinsic activity from the MoS_2 nanosheets compared to Pt is clearly visible from the TOF values. When compared to platinum nanoparticles, MoS_2 nanosheets demonstrated excellent performance with notably lower onset potential and similar TOF values at lower applied potentials. A TOF of 0.1 s^{-1} is achieved for an applied potential of 1258 mV vs. NHE in the case of 1T' MoS_2. This potential is 73 mV and 180 mV smaller than the potential for achieving similar activity from 2H MoS_2 and Pt nanoparticles, respectively.

To gain further understanding on the origin of the high activity of MoS_2 towards DMS oxidation, we computed the binding energy (E_b in eV) of DMS adsorption for different levels of DMS coverage on MoS_2 and Pt(111) surfaces using density functional theory (See "Calculation of the binding energy (E_b) of DMS" section in Supporting Information and **Figure S12**). **Figure 6c** shows the binding energy of DMS on MoS_2 and Pt surfaces as a function of the coverage fraction. In the dilute limit, we found that approximate potentials of 0.46 and 2.56 eV are required to desorb DMS from MoS_2 and Pt, respectively. Charge density differences and Bader charge analysis show that DMS is charge donor in both cases and that the charge transfer (from DMS to the surface) is of +0.18e and +0.38e when DMS is adsorbed on MoS_2 and Pt, respectively (**Figure S13**). Moreover, the shortest distance between an atom of the DMS and an atom of the catalyst is 3.0 Å and 2.3 Å for MoS_2 and Pt, respectively. These key figures demonstrate the strong interaction between DMS and Pt by contrast to mild physisorption of DMS on MoS_2. Interestingly, we found the bonding energy to be -0.55 and -0.90 eV at the edges of the 1T' and 2H phases respectively (**Figure 6d** and **Table S2**). Our DFT calculations suggest that DMS preferentially physisorbs at both the edges and the surface sites of the 1T' MoS_2 nanosheets, leading to more efficient oxidation to DMSO. We anticipate that the strong DMS adsorption in the case of the 2H phase lowers the performance and stability of the 2H phase. Our DFT calculations combined with the examination of the structure of the DMSOR demonstrate that the superior activity from the MoS_2 nanosheets originates from its biomimetic structure and composition. Overall, our results reveal the superior activity of the 1T' phase toward the oxidation of organic sulfide. The activation of the MoS_2 nanosheets originates from the lower binding energy of the

DMS compared to that of platinum. The 1T' phase of MoS_2 is expected to be active from both the edges and the basal planes while the active sites from the 2H phase are localized only on the basal planes due to the larger binding energy on the 2H edge sites. Further calculations of the free energy of the overall DMS oxidation reaction that would provide additional information on the reaction pathways are currently ongoing in our group, but are beyond the scope of this study. Besides the thermodynamics of the reaction, the metallic nature of the 1T' phase of MoS_2 is expected to further improve the kinetics of the reaction and is responsible for the reduction of the overpotentials. Similar behavior has previously been reported in the case of the hydrogen evolution reaction on the 1T' phase of group-6 TMDs.[35] This is supported by the reduced Tafel slope of 75 mV dec^{-1} and the low charge transfer resistance R_{CT} of 370 Ω.

Role of defects and crystallinity of MoS_2 on the DMS oxidation

Defect engineering of MoS_2 has been explored to trigger the electrocatalytic reactions such as the hydrogen evolution reaction or the splitting water.[43,44] To further understand the origin of the MoS_2 activity toward the oxidation of DMS, we prepared electrodes with increasing density of defects. The defect concentration was tuned by thermally annealing MoS_2 under hydrogen atmosphere at increasing temperatures in order to create point-defect vacancies (2H MoS_2-Vs) and sulfur stripping defects (2H MoS_2-Ss) corresponding to low and high defect densities respectively.[45] We also prepared amorphous MoS_2 (A-MoS_x) nanosheets grown under hydrothermal conditions in DMF (See details in Supporting Information). The structure and the composition of the MoS_2 electrodes were analyzed by using Raman and XPS spectroscopy (**Figure S16**). The sulfur-to-molybdenum ratios were estimated to 2.24, 1.79 and 0.63 for A-MoS_x, 2H MoS_2-V_S and 2H MoS_2-S_S respectively. **Figure 7a,b** shows the DMS oxidation performance of the different electrodes compared with the 1T' and 2H phases of MoS_2. We also estimated the electrochemically active surface area (ECSA) by measuring the electrochemical double layer capacitance. The corresponding ECSA-normalized polarization curves are presented in **Figure 7c**. The geometrical current density is found to be the highest for A-MoS_2 along with 1T' MoS_2, while the activity of the 2H phase increases with the concentration of sulfur vacancies. Conversely, J_{ECSA} sharply decreases for A-MoS_x suggesting that the large geometrical current density is ascribed to the more porous or rough nature of the materials. Our results also demonstrate that the performance from defective 2H MoS_2 is comparable to that of its pristine counterpart. We further calculated the binding energy of DMS on the basal plane of 1T' and 2H MoS_2 with single sulfur vacancies (Figure S13, Table S2) and found that, for the same phase, the thermodynamics of the adsorption of DMS is virtually identical on defect-free MoS_2 and MoS_2-V_S basal planes.

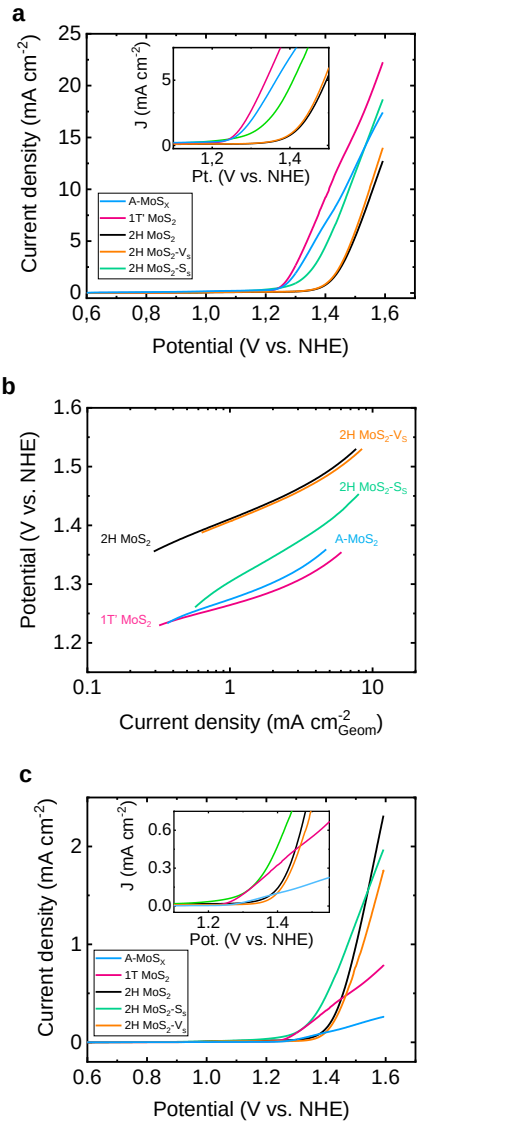

Figure 7. *Electrocatalytic behavior of amorphous MoS_x and defective MoS_2 electrodes towards the oxidation of DMS. (a,b) Polarization curves (a) and corresponding Tafel plots (b) of the different molybdenum sulfide electrodes. Scan rate: 20 mV s^{-1}. (c) ECSA-normalized (J_{ECSA}) polarization curves of amorphous MoS_x and defective MoS_2 electrodes toward the oxidation of DMS compared to the pristine 1T' and 2H phases of MoS_2. Inset: Magnification of the low potential region.*

DMS oxidation mechanism from 1T' MoS_2 nanosheets

Previous reports on the oxidation of DMS have suggested that the reaction proceeds through a one (DMSO) or two electrons ($DMSO_2$) processes.[38,46,47] Instead, our results demonstrate that the DMS is selectively electrochemically oxidized into DMSO *via* a one-electron reaction on both Pt and MoS_2. We anticipate that the oxidation of DMS involves the formation of a radical cation after the electron withdrawal from DMS: $(CH_3)_2S \rightarrow (CH_3)_2S^{\cdot+} + e^-$ as proposed by Elinson and Simonet.[23] The first hint of the presence of radicals during the DMS oxidation is brought by the appearance of light-yellow color in the electrolyte in absence of oxygen during the reaction (**Figure S17**). To further point out the role of radicals during the

reaction, we performed electron paramagnetic resonance (EPR) to detect the formation of sulfur radicals as reaction intermediates. The electro-oxidation of DMS was performed in the presence and in the absence of a radical trapping agent: 5,5-Dimethyl-1-pyrroline N-oxide, DMPO (See "EPR measurements" section in the Supporting Information). First, we performed the reaction in the absence of DMS and no free radical signals were detected. In the presence of DMS, clear EPR signatures are identified centered around 3510 G and the intensity of the signals increases with time (**Figure 8a**). The EPR measurements after 30 min revealed a six-line spectrum different from the spectrum of oxidized radical trapping agent ruling out any oxidation of DMPO.[48] The spectrum corresponds to hyperfine coupling constants of a_N = 15.4 G, a_H = 21 G (g = 2.0621) – close

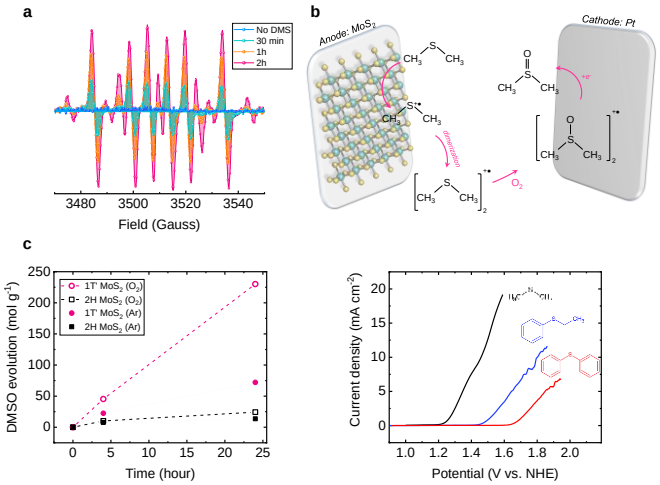

Figure 8. *Mechanism of the electrochemical oxidation of DMS. (a) EPR spectra from the electrolyte in presence of radical trapping agent (DMPO) with absence of DMS (black, blank experiment) and after 30 min (orange), 1 h (blue) with presence of DMS. (b) Proposed mechanism for the reaction of DMS oxidation in O_2 saturated solution. (c) Comparison of the DMSO production from 1T' and 2H MoS_2 in presence or absence of O_2 dissolved in the electrolyte.*

to the constants obtained when trapping $CH_3S^{\cdot -}$ using DMPO: a_N = 15.03 G and a_H = 18 G.[49] Our EPR investigation thus points out that the oxidation of DMS involves the formation of an alkyl sulfur radical that further reacts with DMPO. The additional signals detected after 1h are attributed to the reduction of the DMPO (a_N = 14.5 G, a_H = 19.5 G, see details of the reaction mechanism in the Supporting Information).[50] The sulfur radical cations formed on MoS_2 nanosheets thus act as a "cation pool" in the formation of DMSO as observed for other anodic oxidation reactions in electrosynthesis.[51,52] We propose that the sulfur radicals then reacts with the radical superoxide $O_2^{-\cdot}$ formed at the cathode as previously proposed for the oxidation of thioethers (**Figure 8b** and **Figure S19**).[53] To further confirm the role of oxygen in the reaction, we performed the same reaction under a flow of argon instead of oxygen. After 24 hours, the production rate of DMSO from the 1T' and 2H MoS_2 nanozymes decreases from 680 and 71 L h^{-1} g^{-1} to only 213 and 38 L h^{-1} g^{-1} for the 1T' and 2H MoS_2 respectively (**Figure 8c**). We also found that the Faradic efficiency decreased at higher applied potential (*i.e.* at higher current density) due to the limited concentration of O_2 dissolved in the electrolyte. To generalize our approach, MoS_2 nanosheets have been tested toward the oxidation of different alkyl and aryl sulfide molecules. Our investigations show that ethyl phenyl sulfide and diphenyl sulfide can be oxidized using 1T' MoS_2 2D nanozymes and the onsetpotential associated with the reaction is found to increase when replacing alkyl chains for aryl groups revealing differences in term of reactivity (**Figure 8d**).

Conclusions

Our findings reveal the potential of phase engineered TMDs as biomimetic electrocatalysts for the electrochemical oxidation of sulfide-based molecules. We identified the exfoliated MoS_2 nanosheets as efficient two-dimensional electrocatalysts for the oxidation of alkyl and aryl sulfides. Remarkably, the metallic 1T' phase of MoS_2 exhibits superior activity towards the production of DMSO from DMS compared to noble metals such as platinum nanoparticles and dirhodium complexes with reduced onset potential and lower Tafel slope. By carefully estimating the density of active sites, we determined that the TOF reaches 0.87 s^{-1} at a potential of 1400 mV vs. NHE, 30-fold larger than for polycrystalline platinum (≈ 0.03 s^{-1}). The reaction proceeds *via* one-electron transfer and the Faradaic efficiency is found to be stable for at least 24 hours. We believe that our results open avenues for novel applications of TMDs towards electrochemical-assisted synthesis of organic molecules.

Conflicts of interest

There are no conflicts to declare.

Acknowledgements

D.V., L.M. and K.Q. acknowledge funding from the European Research Council (ERC) under the European Union's Horizon 2020 research and innovation programme (grant agreement No 804320). D.V. and Z.Q. acknowledge financial support from the US Army RDECom Grant N°W911NF-17-2-0033. H.E.M. acknowledges the French embassy in Egypt. N.O. thanks The Hong Kong Polytechnic University and the department of Applied Physics for the computational resources. L.L. acknowledges National Natural Science Foundation of China (21978111) and Zhejiang Provincial Natural Science Foundation of China (LY19B030005).

Notes and references

1 P. K. Robinson, *Essays Biochem*, 2015, **59**, 1–41.
2 J. R. Knowles, *Nature*, 1991, **350**, 121–124.
3 S. J. Benkovic and S. Hammes-Schiffer, *Science*, 2003, **301**, 1196–1202.
4 J. M. Le and K. L. Bren, *ACS Energy Lett.*, 2019, **4**, 2168–2180.

5 B. Hinnemann, P. G. Moses, J. Bonde, K. P. Jørgensen, J. H. Nielsen, S. Horch, I. Chorkendorff and J. K. Nørskov, *J. Am. Chem. Soc.*, 2005, **127**, 5308–5309.

6 H. Wei and E. Wang, *Chem. Soc. Rev.*, 2013, **42**, 6060–6093.

7 J. Wu, X. Wang, Q. Wang, Z. Lou, S. Li, Y. Zhu, L. Qin and H. Wei, *Chem. Soc. Rev.*, 2019, **48**, 1004–1076.

8 L. Gao, J. Zhuang, L. Nie, J. Zhang, Y. Zhang, N. Gu, T. Wang, J. Feng, D. Yang, S. Perrett and X. Yan, *Nature Nanotech*, 2007, **2**, 577–583.

9 F. Natalio, R. André, A. F. Hartog, B. Stoll, K. P. Jochum, R. Wever and W. Tremel, *Nature Nanotech*, 2012, **7**, 530–535.

10 Q. Wang, X. Zhang, L. Huang, Z. Zhang and S. Dong, *Angew. Chem. Int. Ed. Engl.*, 2017, **56**, 16082–16085.

11 Y. Liu, D. L. Purich, C. Wu, Y. Wu, T. Chen, C. Cui, L. Zhang, S. Cansiz, W. Hou, Y. Wang, S. Yang and W. Tan, *J. Am. Chem. Soc.*, 2015, **137**, 14952–14958.

12 Y. Lin, J. Ren and X. Qu, *Acc. Chem. Res.*, 2014, **47**, 1097–1105.

13 S. Ghosh, P. Roy, N. Karmodak, E. D. Jemmis and G. Mugesh, *Angew. Chem. Int. Ed. Engl.*, 2018, **57**, 4510–4515.

14 D. Voiry, H. S. Shin, K. P. Loh and M. Chhowalla, *Nature Reviews Chemistry*, 2018, **2**, 0105.

15 D. Voiry, J. Yang and M. Chhowalla, *Advanced Materials*, 2016, **28**, 6197–6206.

16 X. J. Chua, J. Luxa, A. Y. S. Eng, S. M. Tan, Z. Sofer and M. Pumera, *ACS Catal.*, 2016, **6**, 5724–5734.

17 B. Mohanty, M. Ghorbani-Asl, S. Kretschmer, A. Ghosh, P. Guha, S. K. Panda, B. Jena, A. V. Krasheninnikov and B. K. Jena, *ACS Catal.*, 2018, **8**, 1683–1689.

18 T. J. Johnson and D. D. Hedge, *Am J Health Syst Pharm*, 2002, **59**, 1333–1339.

19 K. P. Garnock-Jones, S. Dhillon and L. J. Scott, *CNS Drugs*, 2009, **23**, 793–803.

20 E. G. Mata, *Phosphorus, Sulfur, and Silicon and the Related Elements*, 1996, **117**, 231–286.

21 C. O. Kinen, L. I. Rossi and R. H. de Rossi, *J. Org. Chem.*, 2009, **74**, 7132–7139.

22 P. T. Cottrell and C. K. Mann, *J. Electrochem. Soc.*, 1969, **116**, 1499–1503.

23 M. N. Elinson and J. Simonet, *Journal of Electroanalytical Chemistry*, 1992, **336**, 363–367.

24 J. V. Lauritsen, M. V. Bollinger, E. Lægsgaard, K. W. Jacobsen, J. K. Nørskov, B. S. Clausen, H. Topsøe and F. Besenbacher, *Journal of Catalysis*, 2004, **221**, 510–522.

25 X. Chen, C. McGlynn and A. R. McDonald, *Chem. Mater.*, 2018, **30**, 6978–6982.

26 Z. Chen, C. Liu, J. Liu, J. Li, S. Xi, X. Chi, H. Xu, I.-H. Park, X. Peng, X. Li, W. Yu, X. Liu, L. Zhong, K. Leng, W. Huang, M. J. Koh and K. P. Loh, *Advanced Materials*, 2020, **32**, 1906437.

27 P. M. Wood, *FEBS Letters*, 1981, **124**, 11–14.

28 P. Joensen, R. F. Frindt and S. R. Morrison, *Materials Research Bulletin*, 1986, **21**, 457–461.

29 G. Eda, H. Yamaguchi, D. Voiry, T. Fujita, M. Chen and M. Chhowalla, *Nano Lett.*, 2011, **11**, 5111–5116.

30 G. Eda, T. Fujita, H. Yamaguchi, D. Voiry, M. Chen and M. Chhowalla, *ACS Nano*, 2012, **6**, 7311–7317.

31 D. Voiry, M. Salehi, R. Silva, T. Fujita, M. Chen, T. Asefa, V. B. Shenoy, G. Eda and M. Chhowalla, *Nano Lett.*, 2013, **13**, 6222–6227.

32 J. Pu, Y. Yomogida, K.-K. Liu, L.-J. Li, Y. Iwasa and T. Takenobu, *Nano Lett.*, 2012, **12**, 4013–4017.

33 M. Acerce, D. Voiry and M. Chhowalla, *Nature Nanotechnology*, 2015, **10**, 313–318.

34 L. Zhao, H. Zhang and Y. Wang, *J. Org. Chem.*, 2016, **81**, 129–136.

35 D. Voiry, R. Fullon, J. Yang, C. de C. C. e Silva, R. Kappera, I. Bozkurt, D. Kaplan, M. J. Lagos, P. E. Batson, G. Gupta, A. D. Mohite, L. Dong, D. Er, V. B. Shenoy, T. Asefa and M. Chhowalla, *Nat Mater*, 2016, **15**, 1003–1009.

36 C. L. Green and A. Kucernak, *J. Phys. Chem. B*, 2002, **106**, 1036–1047.

37 L. Tao, Z. Huo, Y. Ding, Y. Li, S. Dai, L. Wang, J. Zhu, X. Pan, B. Zhang, J. Yao, M. K. Nazeeruddin and M. Grätzel, *J. Mater. Chem. A*, 2015, **3**, 2344–2352.

38 P. T. Cottrell and C. K. Mann, *J. Electrochem. Soc.*, 1969, **116**, 1499–1503.

39 I. Barnes, J. Hjorth and N. Mihalopoulos, *Chem. Rev.*, 2006, **106**, 940–975.

40 G. Liu, Z. Li, J. Shi, K. Sun, Y. Ji, Z. Wang, Y. Qiu, Y. Liu, Z. Wang and P. Hu, *Applied Catalysis B: Environmental*, 2020, **260**, 118134.

41 Y. Zhang, H. Sun, Y. Qiu, X. Ji, T. Ma, F. Gao, Z. Ma, B. Zhang and P. Hu, *Carbon*, 2019, **144**, 370–381.

42 T. F. Jaramillo, K. P. Jørgensen, J. Bonde, J. H. Nielsen, S. Horch and I. Chorkendorff, *Science*, 2007, **317**, 100–102.

43 J. Xie, H. Zhang, S. Li, R. Wang, X. Sun, M. Zhou, J. Zhou, X. W. (David) Lou and Y. Xie, *Advanced Materials*, 2013, **25**, 5807–5813.

44 H. Li, C. Tsai, A. L. Koh, L. Cai, A. W. Contryman, A. H. Fragapane, J. Zhao, H. S. Han, H. C. Manoharan, F. Abild-Pedersen, J. K. Nørskov and X. Zheng, *Nat Mater*, 2016, **15**, 48–53.

45 L. Li, Z. Qin, L. Ries, S. Hong, T. Michel, J. Yang, C. Salameh, M. Bechelany, P. Miele, D. Kaplan, M. Chhowalla and D. Voiry, *ACS Nano*, 2019, **13**, 6824–6834.
46 M. N. Elinson and J. Simonet, *Journal of Electroanalytical Chemistry*, 1992, **336**, 363–367.
47 M. D. Ryan, J. Yau and M. Hack, *J. Electrochem. Soc.*, 1997, **144**, 1952–1957.
48 J. Marcon, G. Mortha, N. Marlin, F. Molton, C. Duboc and A. Burnet, *Holzforschung*, 2017, **71**, 599–610.
49 M. J. Davies, L. G. Forni and S. L. Shuter, *Chemico-Biological Interactions*, 1987, **61**, 177–188.
50 Y. Gorbanev, R. Soriano, D. O'Connell and V. Chechik, *J Vis Exp*, , DOI:10.3791/54765.
51 J. Yoshida, A. Shimizu and R. Hayashi, *Chem. Rev.*, 2018, **118**, 4702–4730.
52 R. Hayashi, A. Shimizu and J. Yoshida, *J. Am. Chem. Soc.*, 2016, **138**, 8400–8403.
53 C. Ye, Y. Zhang, A. Ding, Y. Hu and H. Guo, *Scientific Reports*, 2018, **8**, 1–6.